Manipulating the topological phase of coupled modes in a plasmonic array via engineering near-field asymmetry: From zigzag arrangement to dielectric substrate

Huizhou Wu,[1] Z. Z. Liu [●],[1,2] G. C. Wei,[3] Q. Zhang,[4] and Jun-Jun Xiao [●][1,5,*]

[1]*College of Electronic and Information Engineering and Shenzhen Engineering Laboratory of Aerospace Detection and Imaging,*
Harbin Institute of Technology (Shenzhen), Shenzhen 518055, China
[2]*Research Center for Advanced Optics and Photoelectronics, Department of Physics,*
College of Science, Shantou University, Shantou 515063, China
[3]*School of Mathematical and Physical Sciences, Wuhan Textile University, Wuhan 430200, China*
[4]*Department of Physics and Optoelectronics, Taiyuan University of Technology, Taiyuan 030024, China*
[5]*College of Integrated Circuit, Harbin Institute of Technology (Shenzhen), Shenzhen 518055, China*

Photonic nanoparticle arrays that exhibit topologically nontrivial phases are often established by arranging nanoparticles in a lattice configuration in analog to the Su-Schrieffer-Heeger model. This design strategy is based on the principle that the optical interactions among the nanoparticles are predominantly dictated by the distances between them. However, these interactions are also significantly shaped by the near-field profiles of the nanoparticles. As an exemplary case, we examine a zigzag array of metallic ellipsoidal nanoparticles (ENPs) and illustrate how the topological phase of coupled plasmonic waves in such an array can be manipulated by controlling the orientation of the ENPs. More intriguingly, the near-field characteristics of the ENPs can be fine-tuned by the presence of a substrate, suggesting an alternative avenue for modulating the inter-particle interactions. We further show that topological phase transitions in both one-dimensional (1D) and 2D ENP arrays can be triggered by introducing a nearby dielectric substrate, while maintaining the original lattice structure unchanged. Our findings reveal a different mechanism for modulating the topological phases of nanoparticle arrays and provide a strategy that could be extrapolated to other photonic and classical wave systems, suggesting possibilities for the design and control of topological states in carefully engineered photonic systems.

I. INTRODUCTION

Over the past decade, topological photonics has become one of the most active research areas in optical field because of the unique properties of photonic topological states, such as the robustness against disorder, which are beyond the realm of conventional photonics [1–7]. Plasmonic nanoparticles are an essential platform for the exploration of topological effects at the nanoscale [8–21]. Analogous to the tight-binding model, nanoparticle arrays with topologically nontrivial plasmonic bands have been successfully realized in a variety of photonic lattices, such as the celebrated Su-Schrieffer-Heeger (SSH) model [8–12], the breathing Kagome lattice [13,14], and breathing honeycomb lattice [16,18,19]. In these studies, the interactions among the nanoparticles were usually determined by the distances between them. As a direct consequence, the topological phase of the nanoparticle arrays was seen to be almost entirely dependent upon the lattice geometry of the arrays.

However, the lattice geometry of photonic lattices, particularly the spatial distance between nanoparticles, is often difficult to reconfigure. This limitation means that the topological phase of an array, and the frequency of its topological states, are typically fixed following the design and fabrication stages, presenting a barrier to the flexible application of topological photonics. This situation prompts a significant question: Is it possible to manipulate the topological phases of photonic lattices without altering their geometric configuration? Several research endeavors have touched on this question. For instance, the topological phase of dipolelike arrays can be tuned by adjusting the polarization of the incident light [22–25] or by structuring the local photonic environment [15,17,26–28]. Additionally, topological transitions in optical waveguide arrays have been realized through the combination of different modes [29,30], topological states can also be controlled by inducing a dielectric change in the constituent materials [31].

Approximately, the electromagnetic interactions among nanoparticles originate from the interplay of their near fields, which are influenced not only by the distance separating the particles but also by the near-field profile of individual nanoparticles [15,21,22,32]. Inspired by this, we propose an alternative option that does not require complex lattice geometry but instead relies on asymmetric near-field profile of nanoparticles to achieve modulation of coupling within nanoparticle array. As an illustrative example, we consider a zigzag array of metallic ellipsoidal nanoparticles (ENPs), wherein the near-field distributions are governed by the orientation of the ENPs. We demonstrate that topological phase

---

*Contact author: eiexiao@hit.edu.cn

transitions in the equidistant array can be induced by simply reorienting the major axis of the ENPs. Furthermore, the near-field characteristics of nanoparticles can be finely modulated by the presence of substrates [33–38], providing a practical avenue to tailor the interactions within nanoparticle arrays. More crucially, as we prove in this paper, the intracell and intercell coupling dynamics of a periodic array of ENPs can be effectively modified by introducing a homogeneous dielectric substrate. This enables the substrate to dynamically control the topological phase of coupled waves in nanoparticle arrays, thereby eliminating the necessity to alter the lattice structure.

While we have focused on 1D chains and 2D kagome arrays of ENPs, the principle of controlling interactions through the manipulation of near-field profiles is extendable to more complex nanoparticle arrays [37–39]. Moreover, the phenomenon of substrate influencing local field distributions is also observed in a range of classical wave systems, such as optical waveguides [30], dielectric resonators [33,37], atomic arrays [40,41], and phononic crystals [42]. Therefore, we expect our proposal could not only provide an alternative way to induce topological phase transitions in nanoparticle arrays but also inspire unique methods for controlling topological phases in other classical wave systems.

II. TOPOLOGICAL PHASE TRANSITION IN A ZIGZAG ARRAY OF ELLIPSOIDAL NANOPARTICLES

Throughout this paper, we treat silver ENPs with major axis length 20 nm and minor axis length 10 nm as the meta atoms that constitute the array. The ENP supports two distinct dipole resonance modes: one where the dipole is aligned with the major axis and another with the minor axis. We only consider the dipole resonance mode associated with the major axis, which occurs near $f = 690$ terahertz (THz), as the minor axis dipole resonance, occurring near $f = 850$ THz, is sufficiently frequency separated from the primary mode of interest. This separation ensures that the two modes can be controlled and investigated independently. More details regarding the optical response of an individual silver ENP are provided in Appendix A.

We now consider a periodic equidistant array as shown in Fig. 1(a), which is composed of two ENPs within each unit cell, distinguished as A and B. The centers of A and B are positioned at equal spacings of 30 nm along the x axis while having an offset of 10 nm in the y direction. The major axes of A and B are arranged in the xy plane and make the same angle of φ with respect to the positive direction of the x axis. Despite the uniform center-to-center distances in the equidistant array, the couplings between adjacent ENPs can exhibit distinct characteristics, which can be effectively modulated by altering φ. Figure 1(b) schematically depicts the near-field distributions of the array for different φ, in which the ENPs are symbolically replaced by red arrows that represent the equivalent dipoles. When $\varphi = 45°$, the overlap between the near fields of each A with the adjacent B on its left is distinct from the overlap with the adjacent B on its right, as illustrated in the first row of Fig. 1(b). The unequal near-field overlap on either side of each ENP leads to a staggered coupling effect within the equidistant array. This is distinct from Ref. [21], wherein the ENPs are arranged linearly, and thus the
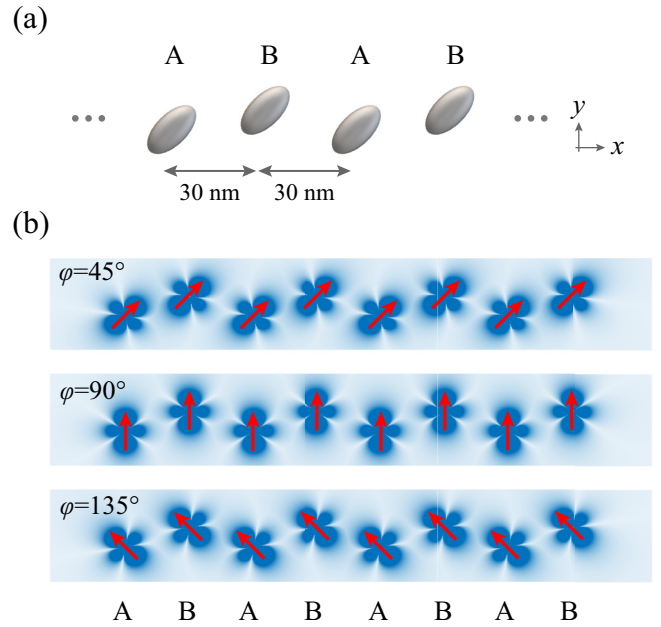

FIG. 1. (a) Schematic of the zigzag array of silver ENPs. (b) The near-field distributions of the array with different φ. The darker the color, the stronger the corresponding field intensity.

coupling between any two adjacent ENPs remains consistent as long as the orientations of the ENPs within the unit cell are uniform. In our case, the ENPs form an equispaced zigzag array. The coupling between any two adjacent ENPs in this array is identical only when $\varphi = 0°$ or $90°$. At the specific orientations, the overlap of the near fields between any two adjacent ENPs becomes consistent, as depicted in the second row of Fig. 1(b). This consistency in near-field overlap ensures that the nearest-neighbor coupling throughout the array is uniform. In addition, when $\varphi = 135°$ [the third row in Fig. 1(b)], the near-field overlap between adjacent ENPs demonstrates a pattern that is precisely the inverse of the case of $\varphi = 45°$. This reversal in near-field overlap has the potential to induce a topological phase inversion within the array. Notably, this phenomenon is observed for any pair of φ that are complementary to each other.

To systematically analyze and quantify the couplings within the array, we adopt a simplified model by treating the ENPs as point dipoles. Under this approximation, the optical responses of such an array can be accurately described by a set of coupled dipole equations [21,43]

$$\frac{1}{\alpha(\omega)}\mathbf{p}_n = E_0 + \frac{\omega^2}{c^2}\sum_{m \neq n}\mathbf{M}(\mathbf{x}_n - \mathbf{x}_m, \omega)\mathbf{p}_m, \qquad (1)$$

where $\mathbf{p}_{n,m}$ and $\mathbf{x}_{n,m}$ represent the dipole moments and positions of the n, mth ENP in the array, respectively. In Eq. (1), α, ω, c, and E_0 are the polarizability of the ENP (see Appendix A), the angular frequency, the speed of light in free space, and the external incident field, respectively. Note that M describes the interaction between the nth and mth ENPs, and is given by

$$\mathbf{M}(\mathbf{x}_n - \mathbf{x}_m, \omega) = [\overset{\leftrightarrow}{\mathbf{G}}(\mathbf{x}_n - \mathbf{x}_m, \omega) \cdot \mathbf{I}_m]^T \cdot \mathbf{I}_n, \qquad (2)$$
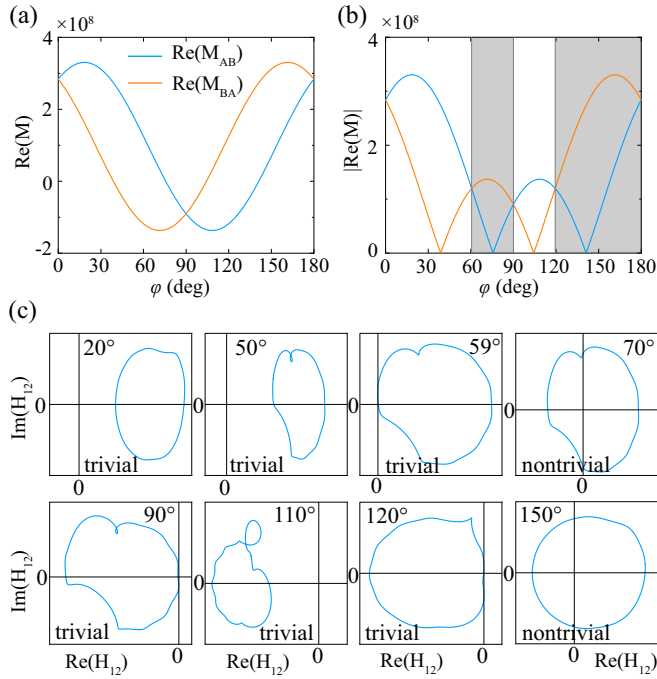
FIG. 2. (a) Real part of M_{AB} and M_{BA} which describe the intra- and intercoupling of the array, respectively. (b) The absolute value of real part of M_{AB} and M_{BA}, shown by the blue and yellow lines, respectively. The gray shaded areas correspond to $\varphi \in (60.5°, 90°) \cup (119.5°, 180°)$. (c) The winding of H_{12} with different φ.

where $\mathbf{I}_{n,m} = [\cos\varphi \, \sin\varphi \, 0]^T$ represents the unit vector in the direction of the major axis of the ENP and T denotes the transpose operation. Here $\overset{\leftrightarrow}{\mathbf{G}}$ refers to the free space dyadic Green's function and is given by

$$\overset{\leftrightarrow}{\mathbf{G}}(\mathbf{r}, \omega) = \frac{e^{ikr}}{r}\left[\left(1 + \frac{i}{kr} - \frac{1}{k^2r^2}\right)\overset{\leftrightarrow}{\mathbf{I}} - \left(1 + \frac{3i}{kr} - \frac{3}{k^2r^2}\right)\mathbf{n} \otimes \mathbf{n}\right], \quad (3)$$

where $\mathbf{r}$ is the position vector, with $r = |\mathbf{r}|$ and $\mathbf{n} = \mathbf{r}/r$. Here $\overset{\leftrightarrow}{\mathbf{I}}$ and $k = \omega/c$ are the identity matrix and the free space wave number, respectively. The intracoupling (intercoupling) of the array can be described by the interaction between A and adjacent B on its right (left)

$$M_{AB} = \left[\overset{\leftrightarrow}{\mathbf{G}}(\Delta\mathbf{x}, \omega) \cdot \mathbf{I}_B\right]^T \cdot \mathbf{I}_A$$

$$M_{BA} = \left[\overset{\leftrightarrow}{\mathbf{G}}(\Delta\mathbf{x} - \mathbf{d}, \omega) \cdot \mathbf{I}_B\right]^T \cdot \mathbf{I}_A, \quad (4)$$

where $\mathbf{I}_A = \mathbf{I}_B = [\cos\varphi \, \sin\varphi \, 0]^T$, $\Delta\mathbf{x}$ is the position vector between A and B in a unit cell, $\mathbf{d}$ is the lattice unit vector.

Figure 2(a) shows the computed real part of M_{AB} and M_{BA}. As expected, they are equal only when $\varphi = 0°$ or $90°$ ($180°$ is equivalent to $0°$). Figure 2(b) presents a plot of the intracoupling and intercoupling strengths of the array. The gray shaded areas [$\varphi \in (60.5°, 90°) \cup (119.5°, 180°)$], which can be effectively controlled by the y offset, denote conditions where the intercoupling is stronger than the intracoupling.

Under the nearest-neighbor approximation [8,18], these gray shaded areas are associated with the nontrivial topological phase, while the remaining regions correspond to the trivial topological phase.

To go beyond the nearest-neighbor approximation, we consider an infinite periodic equidistant array. By applying the Bloch's theorem for the infinitely array with zero incident field, the coupled dipole equations can be converted into the following eigenequation:

$$\left[\frac{1}{\alpha(\omega)}\overset{\leftrightarrow}{\mathbf{I}} - \overset{\leftrightarrow}{\mathbf{H}}\right]\mathbf{P} = \mathbf{0}, \quad (5)$$

where $\mathbf{P} = [p_A, p_B]^T$. The 2×2 effective Hamiltonian $\overset{\leftrightarrow}{\mathbf{H}}$ has elements as the following:

$$H_{11} = \frac{\omega^2}{c^2}\sum_{n\in Z, n\neq 0} M(n\mathbf{d}, \omega)e^{ik_x nd},$$

$$H_{12} = \frac{\omega^2}{c^2}\sum_{n\in Z} M(n\mathbf{d} + \Delta\mathbf{x}, \omega)e^{ik_x nd},$$

$$H_{21} = \frac{\omega^2}{c^2}\sum_{n\in Z} M(n\mathbf{d} - \Delta\mathbf{x}, \omega)e^{ik_x nd},$$

$$H_{22} = \frac{\omega^2}{c^2}\sum_{n\in Z, n\neq 0} M(n\mathbf{d}, \omega)e^{ik_x nd}, \quad (6)$$

where k_x is the Bloch momentum. The effective Hamiltonian is non-Hermitian due to the prominent radiative and retardation effects from dipole-dipole interactions within the plasmonic array [10,11,19]. The topological characteristics of such a non-Hermitian 1D system are linked to the complex Zak phase, which can be described by the winding number of the off-diagonal Hamiltonian elements, H_{12} or H_{21}, as they encircle the origin of the complex plane across the first Brillouin zone, multiplied by π [11,44]. We have computed the winding number of H_{12} at different φ. Figure 2(c) presents the results for several representative cases. It is observed that the winding number of H_{12} shifts from zero to one (or one to zero) near $\varphi = 59°$, $90°$, and $121°$, which correspond to the topological phase transition points illustrated in Fig. 2(b). We note that they are not completely consistent due to the interactions beyond the nearest neighbor. This indicates that the topological properties of the array can be precisely controlled through the manipulation of the near-field overlap among nanoparticles, despite the presence of non-Hermitian effects and long-range dipolar interactions within the array.

To further verify the topological phase transitions in the array, we have conducted full-wave simulations using a finite element method (FEM) solver (COMSOL Multiphysics). Figure 3(a) shows the simulated eigenmodes of a finite equidistant array with varying φ. As predicted by the winding number of H_{12}, edge states are present only when $\varphi \in (59°, 90°) \cup (121°, 180°)$. Figures 3(b) and 3(c) show the electric field intensity distributions of the double degenerate edge states of the array for $\varphi = 70°$ and $130°$, respectively. We note that the edge states are not symmetry protected because the chiral symmetry of the array is broken by the couplings beyond nearest neighbors.
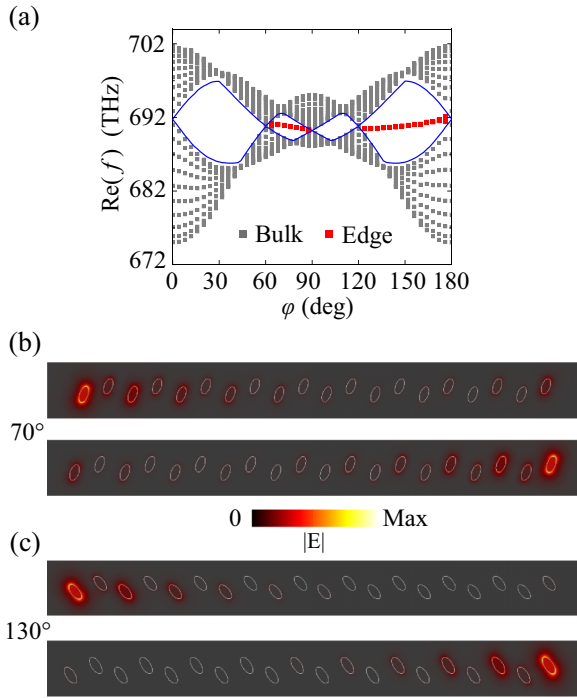
FIG. 3. FEM full-wave simulations. (a) eigenmodes of a ten-unit-cell equidistant array with varying φ. Edge states exist when $\varphi \in (59°, 90°) \cup (121°, 180°)$. The blue lines are gap boundaries calculated under the Bloch boundary condition. (b) Electric field intensity distributions of the degeneracy edge states of the array with $\varphi = 70°$; the frequency is $f = 689.0$ THz. The white ellipses represent the positions of ENPs. (c) Same as (b) but with $\varphi = 130°$; the frequency is $f = 688.5$ THz.

III. SUBSTRATE-INDUCED TOPOLOGICAL PHASE TRANSITIONS

In this section, we explore how to induce topological phase transitions in ENP arrays using a dielectric substrate. Prior to constructing the array, it is necessary to understand how the substrate affects the near-field of an individual ENP. Due to the geometric symmetry of the ENP, the near-field distribution of an ENP in the dipole mode is inherently symmetric about its center. However, when a substrate is introduced close to it, the near field produced by the ENP interacts with the inhomogeneous field reflected from the substrate, which disrupts the symmetrical nature of the dipole mode profiles. For illustration, consider an ENP positioned near a dielectric substrate with its major axis inclined relative to the substrate's surface. In this arrangement, the dipole mode profile of the ENP becomes asymmetric due to the substrate's influence, as depicted in Fig. 4(a). The distribution of the asymmetric field can be precisely adjusted by altering the properties of the substrate, which provides an effective strategy for tailoring ENP couplings in arrays, eliminating the need to alter interparticle distances.

We now focus on a chain of ENPs positioned near a dielectric substrate, as shown in Fig. 4(b). The substrate is sufficiently thick to be regarded as semi-infinite. The chain consists of two types of ENPs with different orientations, labeled A and B. The major axes of A and B are oriented at
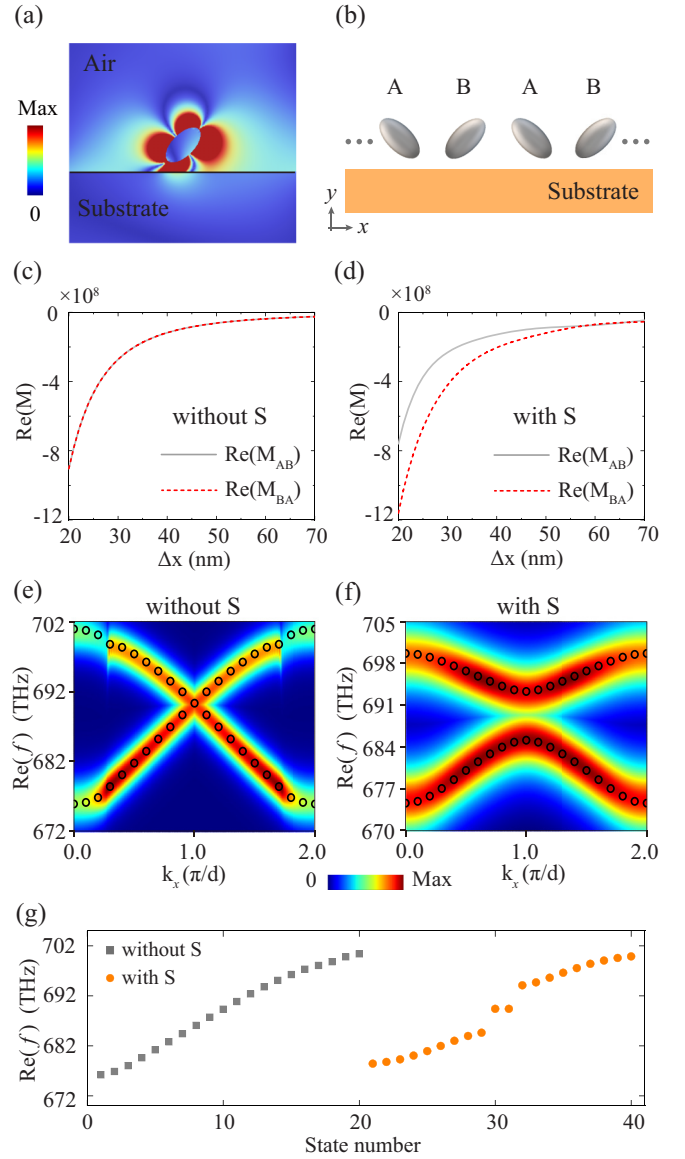

FIG. 4. (a) The dipole mode profile of an ENP situated near a dielectric substrate with the permittivity $\epsilon_{sub} = 10$. The center of ENP is located 12 nm above the substrate. (b) Schematic of a chain of ENPs close to the dielectric substrate. (c) The intra- and intercoupling of the chain without the substrate. (d) Same as (c) but with the substrate. (e) The band structures and eigenpolarizability spectrum of the chain with $\Delta x = 30$ nm without the substrate. (f) Same as (e) but with the substrate. (g) Eigenmodes of a finite-sized chain (ten unit cells) without (states 1–20) and with (states 21–40) the substrate, respectively. The S in (c)–(g) represents substrate.

135° and 45°, respectively, with respect to the positive x axis. The particles A and B are uniformly spaced, 12 nm above the substrate, with a consistent center-to-center distance, Δx, between any two adjacent ENPs along the chain. To incorporate the effects of the substrate, we employ the reflecting Green's function $\overset{\leftrightarrow}{\mathbf{G}}_R$ that describes the field reflected by the substrate [36,40,45]. The explicit expression of $\overset{\leftrightarrow}{\mathbf{G}}_R$ is provided in Appendix B. Consequently, the interaction between the nth and

m-th ENPs in the chain is adjusted to

$$M(\mathbf{x}_n - \mathbf{x}_m, \omega)$$
$$= [(\overset{\leftrightarrow}{\mathbf{G}}(\mathbf{x}_n - \mathbf{x}_m, \omega) + \overset{\leftrightarrow}{\mathbf{G}}_R(\mathbf{x}_n - \mathbf{x}_m, \omega)) \cdot \mathbf{I}_m]^T \cdot \mathbf{I}_n. \quad (7)$$

The intra- and intercoupling of the chain in the presence of the substrate have the following form:

$$\mathbf{M}_{AB} = [(\overset{\leftrightarrow}{\mathbf{G}}(\Delta\mathbf{x}, \omega) + \overset{\leftrightarrow}{\mathbf{G}}_R(\Delta\mathbf{x}, \omega)) \cdot \mathbf{I}_B]^T \cdot \mathbf{I}_A,$$

$$\mathbf{M}_{BA} = [(\overset{\leftrightarrow}{\mathbf{G}}(\Delta\mathbf{x} - \mathbf{d}, \omega) + \overset{\leftrightarrow}{\mathbf{G}}_R(\Delta\mathbf{x} - \mathbf{d}, \omega)) \cdot \mathbf{I}_B]^T \cdot \mathbf{I}_A, \quad (8)$$

where $\mathbf{I}_A = [\cos 135° \sin 135° 0]^T$, $\mathbf{I}_B = [\cos 45° \sin 45° 0]^T$, and **d** is the lattice unit vector. The eigenequation of the chain in the presence of the substrate can be obtained by simply replacing the interaction terms in the effective Hamiltonian in Eq. (5) with Eq. (7).

To quantify the influence of the substrate, we have calculated the intra- and intercoupling of the chain both without and with a substrate with the permittivity $\epsilon_{sub} = 10$, utilizing Eqs. (4) and (8), respectively. Figure 4(c) shows the results for an isolated chain in absence of the substrate, demonstrating consistent intra- and intercoupling. In contrast, with the substrate in presence, the strength of the intracoupling becomes weaker than the intercoupling, as illustrated in Fig. 4(d). This alteration leads to the transformation of the plasmonic band structures of the chain from being gapless to gapped. The band structures can be obtained by solving the corresponding eigenequation as well. The black circles in Figs. 4(e) and 4(f) show the band structures of the chain with $\Delta x = 30$ nm in absence and in presence of the substrate, respectively. The appearance of a gap when the substrate is present is clearly observed, which is a direct result of the unequal strength between the intra-coupling and the intercoupling. We have also calculated the effective eigenpolarizability [19,46] of the chain as shown by the contour spectrum in Figs. 4(e) and 4(f), which verifies our results. Further, we consider a finite-sized chain. Figure 4(g) shows the eigenmodes of the chain calculated by the coupled dipole equations. It can be seen that in the presence of the substrate, the bulk gap is open and two in-gap states appeared inside, as expected.

Figure 5 presents the FEM simulations of the chain with $\Delta x = 30$ nm. The FEM band structures depicted in Fig. 5(a) agree with our analytical results obtained under the coupled dipole approximation as shown in Figs. 4(e) and 4(f). Figure 5(b) shows the simulated eigenmodes of a finite chain. The emergence of a pair of topological edge states indicates that the chain has transformed into topologically nontrivial phase due to the presence of the substrate. The edge states can be excited by an evanescent plane wave perpendicular to the *xy* plane, as illustrated in Fig. 5(c)III.

Since the topological nontrivial phase of such a chain relies on the substrate's affection, it is anticipated that the topological edge states can be controlled by the properties of the substrate. Figures 5(d) and 5(e) show the dependence of the band gap and edge states of the ENP chain on the substrate. When the chain-substrate distance Δh is large enough or when ϵ_{sub} approaches the permittivity of the surrounding environment, the light field reflected by the substrate becomes extremely weak. Under such conditions, the intracoupling and
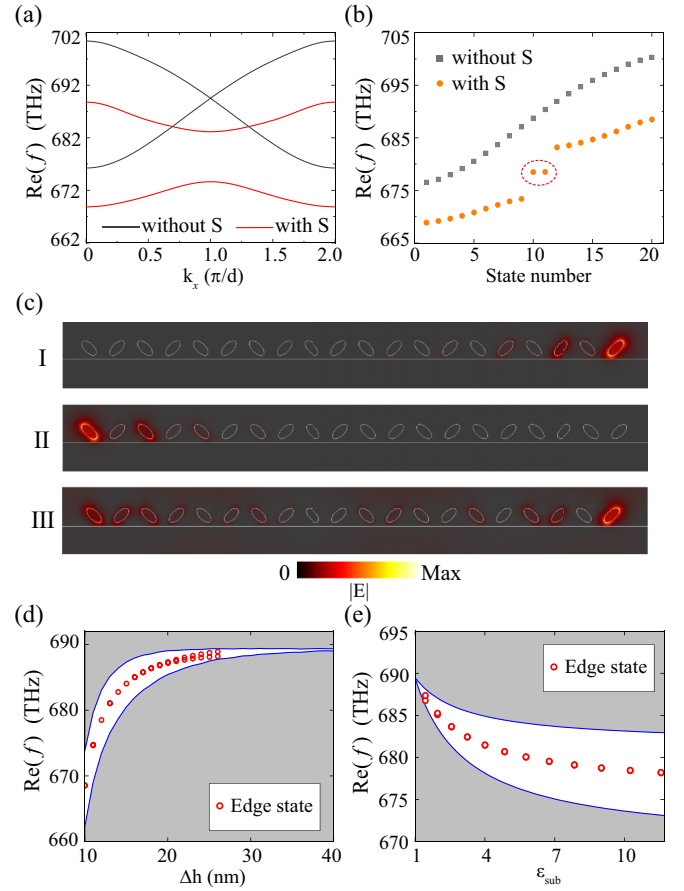

FIG. 5. FEM simulation results of the ENP chain with $\Delta x = 30$ nm. (a) Band structures. (b) Eigenmodes of a finite-sized chain (ten unit cells) without and with the substrate, respectively. (c) panels I and II show the two in-gap states encircled by a dashed oval in (b). Panel III shows the edge state excited by an evanescent plane wave perpendicular to the xy plane polarized along the y axis, with the excitation frequency 678.5 THz. The white lines show the top boundary of the substrate. (d) The band gap and edge states for different Δh with $\epsilon_{sub} = 10$. (e) The band gap and edge states for different ϵ_{sub} with $\Delta h = 12$ nm. The gap boundaries (blue lines) are calculated under the Bloch boundary condition, and the edge states are eigenmodes of a ten-unit-cells ENP chain.

the intercoupling in the chain restore to those as in a bare chain, causing the closing of the band gap. Consequently, the band gap and frequency of the edge states change with the substrate configuration as shown in Figs. 5(d) and 5(e).

To further demonstrate that the topological phase of the plasmonic chain can be manipulated by a substrate, we have designed a contracted and an expanded ENP chain, as depicted in Figs. 6(a) and 6(b), respectively. In the absence of the substrate, the contracted ENP chain is in a trivial phase, as the interactions among ENPs are inversely related to the distance separating them. However, with the substrate present, as illustrated in Fig. 6(a), the intracoupling is diminished while the intercoupling is amplified by the substrate, according to our prior analysis. Clearly, the influence of the substrate on the chain can be effectively tuned by adjusting its characteristics, such as the permittivity and the degree of proximity to the
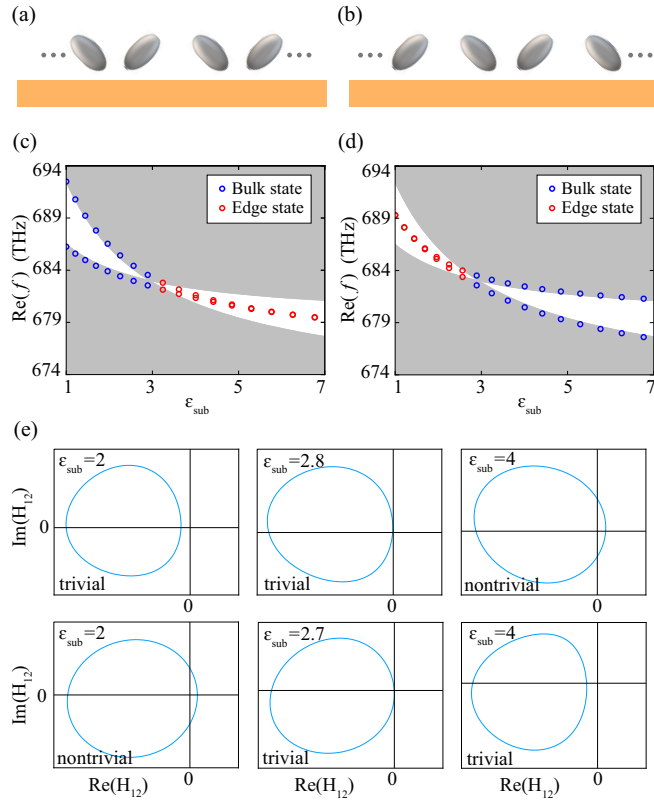
FIG. 6. Topological phase transitions in an ENP chain induced by a dielectric substrate. (a) Schematic of a contracted ENP chain with the substrate. The intradistance (interdistance) is 27.6 nm (32.4 nm). (b) An expanded ENP chain with the substrate. The intradistance (interdistance) is 32.4 nm (27.6 nm). (c) The gray areas highlight the band gap of the contracted chain with varying ϵ_{sub}, calculated under the Bloch boundary condition. The blue and red circles represent the eigenmodes of a 15-unit-cell ENP chain. (d) Same as (c) but for the expanded chain. (e) Winding situation of H_{12} of the contracted (the first row) and the expanded (the second row) ENP chain with the substrate.

chain, which allows us to control the topological phase of the chain.

As depicted in Fig. 6(c), we present the band gap and eigenmodes of a contracted ENP chain in proximity to a dielectric substrate. With the increasing of the permittivity of the substrate, the bulk gap of the chain experiences the process of opening, closing, and reopening. Meanwhile, a pair of bulk states (denoted by blue circles) fall into the bulk gap and gradually evolve to degenerate topological edge states (red circles). This evolution clearly demonstrates that the contracted ENP chain undergoes a topological phase transition from trivial to nontrivial under the influence of the substrate. The field distributions of the two edge (bulk) states corresponding to the substrate with varying permittivity are provided in Appendix C. In addition, in Fig. 6(d), we present the opposite situation where an expanded ENP chain, as shown in Fig. 6(b), transforms from a nontrivial phase to trivial phase as the permittivity of the substrate increases. To conclusively verify the topological phase transitions, we have performed calculations of the complex Zak phases for both the contracted
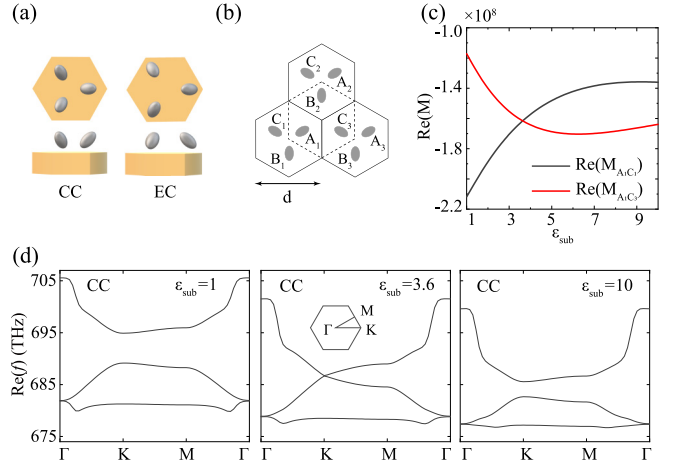

FIG. 7. (a) Schematics of the kagome contracted cell (CC) and kagome expanded cell (EC). The yellow hexagon represents the substrate with $\Delta h = 14$ nm. (b) A kagome array of CCs. The solid hexagons represent the CCs, the dashed hexagon represent the EC. $d = 70$ nm is the lattice constant. (c) The coupling between C_1 (C_3) and A_1 vary with the permittivity of the substrate. (d) FEM band structures of the CC with different ϵ_{sub}.

and expanded chains. Figure 6(e) shows the evolution of the winding number of the two cases with varying permittivity of the substrate, which are consistent with the topological properties shown in Figs. 6(c) and 6(d).

IV. HIGHER-ORDER TOPOLOGICAL MODES INDUCED BY SUBSTRATE

In this section, we show that our proposal can be applied to induce higher-order topological modes in 2D plasmonic arrays. We consider kagome arrays composed of ENPs with a nearby dielectric substrate. Figure 7(a) shows the kagome unit cells; the contracted cell (CC) consists of three ENPs with their major axes oriented in spherical coordinates as $(0, 45°)$ and $(\pm 120°, 45°)$, respectively. The intradistance (interdistance) is 31.5 nm (38.5 nm). For the expanded cell (EC), the orientations of ENPs are $(0, -45°)$ and $(\pm 120°, -45°)$, respectively. The intradistance (interdistance) is 38.5 nm (31.5 nm). This design ensures consistent band gaps between the CC and EC, even in the presence of the substrate. Figure 7(b) shows a kagome lattice composed of CCs. The solid hexagons represent the CCs while the dashed hexagon can represent the EC. The intracoupling (intercouping) is represented by the coupling between C_1 (C_3) and A_1, which is significantly affected by the permittivity of the substrate as shown in Fig. 7(c). It can be seen that the strength of intracoupling is diminished while the intercoupling is amplified by the substrate. In particular, the intracoupling and intercoupling are reversed when $\epsilon_{sub} > 3.6$. Consequently, the CC transforms from the topological trivial phase to the topological nontrivial phase if we introduce the substrate with $\epsilon_{sub} > 3.6$. Figure 7(d) shows the band structures of the CC with different ϵ_{sub}. The band gap undergoes a process of opening, closing, and reopening as the ϵ_{sub} increases. In addition, since the intracoupling and intercoupling of the EC and CC are precisely
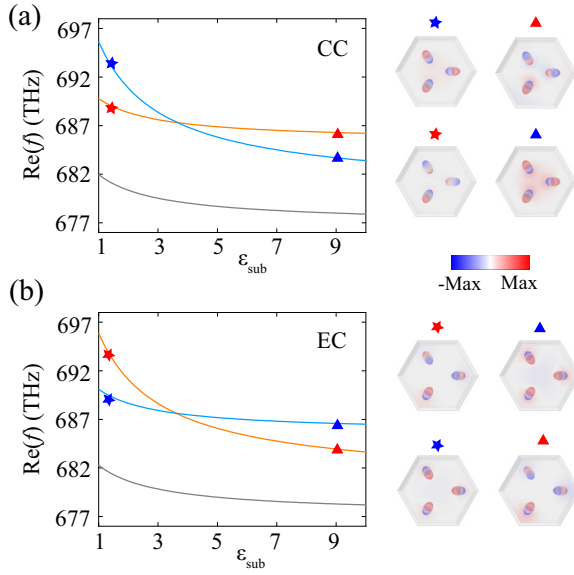
FIG. 8. Frequency evolution of the eigenstates at the K point as the ϵ_{sub} increases. (a) For the CC; (b) for the EC.

FIG. 9. (a) The eigenspectrum of a finite kagome array of CCs with $\epsilon_{sub} = 1$. (b) The eigenspectrum of a finite kagome array of CCs surrounded by ECs, with $\epsilon_{sub} = 10$. (c), (d) Electric field distributions of the in-gap edge and corner states labeled in (b).

swapped, the topological phase of the EC transforms from the nontrivial phase to the trivial phase with the increase in ϵ_{sub}.

To prove the topological phase transitions predicted by Fig. 7(c), we study the eigenstates of the CC and EC at the K point in the first Brillouin zone. Figure 8(a) shows the frequency evolution of the eigenstates of the CC at the K point as the ϵ_{sub} increases. The eigenstates are represented by charge density distribution of ENPs within the unit cell. As the ϵ_{sub} increases, we clearly observe the band inversion between the second and third bands. Particularly, the band inversion appears near $\epsilon_{sub} = 3.6$, which is consistent with our analytical calculations of the topological phase transition point. Figure 8(b) shows the evolution of the eigenstates of the EC. It can be observed that the eigenstates of the second and third bands are reversed for the EC and CC at the same ϵ_{sub}, which indicates that the topological phases of the EC and CC are opposite.

To verify the topological phase transitions induced by the substrate, we now consider finite Kagome arrays composed of the ENPs with a nearby substrate. Figure 9(a) shows the eigenspectrum of a finite Kagome array composed of CCs with $\epsilon_{sub} = 1$. No in-gap states exist because of the trivial topological phase of the CC. Next, we consider the case when ϵ_{sub} is increased to 10. To investigate the higher-order topological modes of this case, we surround the array of CCs with ECs as shown by the inset of Fig. 9(b). The corresponding eigenspectrum includes corner and edge states, which indicates that the CC transitions from the topological trivial phase to the nontrivial phase as ϵ_{sub} is increased.

We note that all the eigenfrequencies presented in this paper have imaginary components as shown in Appendix D. For experimental convenience, the ENP array can be embedded in a uniform medium, such as glass [10,47]. In Appendix E, we discuss the effect of the dielectric constant of surrounding medium. Moreover, it could be of significance to explore unconventional substrates such as multilayer film
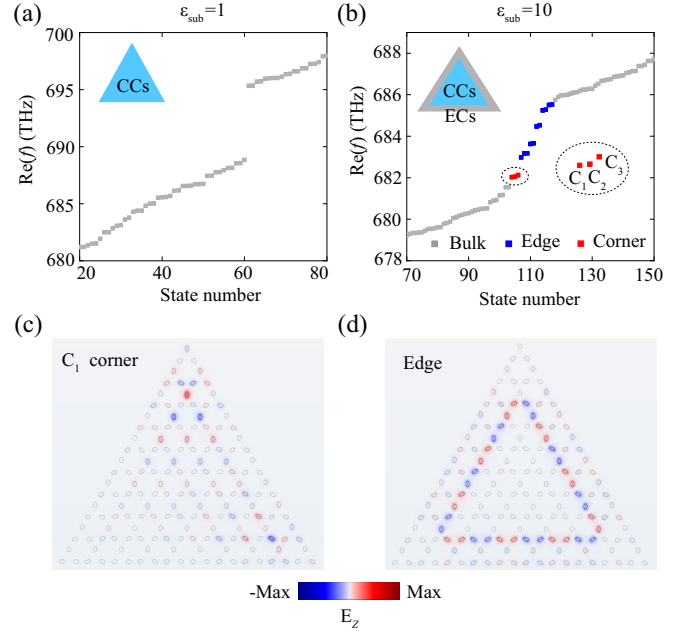
[37], parabolic, or hyperbolic metamaterial [48], etc., since different substrates offer distinct reflective Green's function. We anticipate that these variations could lead to a broad range of complex and intriguing topological transitions.

V. CONCLUSION

In summary, we have shown that interactions among plasmonic nanoparticles can be controlled by shaping their near-field profiles. This insight opens a pathway for controlling the topological phase of nanoparticle arrays. We have demonstrated that the topological phase of a zigzag array of ENPs can be effectively modulated by simply adjusting their common orientation, which directly governs the near-field profile of the ENPs. Furthermore, it is particularly fascinating to observe that the near-field characteristics of ENPs can be finely tuned by the presence of a nearby substrate. We have proved that topological phase transitions in an ENP array can be induced by such a dielectric substrate, bypassing the need for geometrical or material property alterations to the array itself. We envision that our approach offers alternatives for inducing topological phase transitions in topological photonic systems and may inspire creative methods for manipulating topological phases in other classical wave systems.
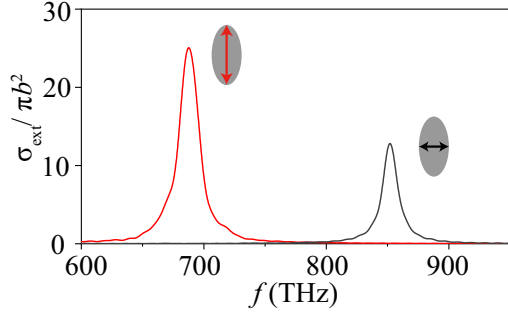
FIG. 10. Extinction cross sections of a silver ENP with major axis half-length $a = 10$ nm and minor axis half-length $b = c = 5$ nm. Red and black curves represent the extinction cross section of the ENP subjected to a light field polarized parallel to and vertical to the major axis, respectively.

APPENDIX A: THE OPTICAL RESPONSE OF AN INDIVIDUAL ENP

Here we give the detailed description of the silver ENP used in the main text. The dielectric function of silver is given by the Drude model as

$$\epsilon(\omega) = \epsilon_\infty - \frac{\omega_p^2}{\omega^2 + i\omega/\tau}, \tag{A1}$$

with $\epsilon_\infty = 5$, $\omega_p = 1.36 \times 10^{16}$ rad/s and $1/\tau = 5.88 \times 10^{13}$ rad/s [49]. Here ω and i represent the working frequency and the imaginary unit, respectively. The polarizability tensor of the ENP is [21]

$$\overset{\leftrightarrow}{\alpha}(\omega) = \begin{bmatrix} \alpha_a(\omega) & 0 & 0 \\ 0 & \alpha_b(\omega) & 0 \\ 0 & 0 & \alpha_c(\omega) \end{bmatrix}, \tag{A2}$$

where α_l ($l \in [a, b, c]$) are the projections of the polarizability tensor in the directions of the axes of the ENP. Considering the radiative effects, we employ the modified long-wavelength approximation to describe α_l as [50]

$$\alpha_l(\omega) = \frac{\alpha_l^s(\omega)}{1 - \frac{Dk^2}{l}\alpha_l^s(\omega) - i\frac{2k^3}{3}\alpha_l^s(\omega)}, \tag{A3}$$

where $D, l, k = \omega/c_0$ and c_0 are the dynamic geometrical factor, axis half-length, wave number, and speed of light in free space. Note that the static polarizabilities α_l^s of the ENP can be written as [21,51]

$$\alpha_l^s(\omega) = \frac{V}{4\pi} \frac{\epsilon(\omega) - \epsilon_b}{\epsilon_b + L_l[\epsilon(\omega) - \epsilon_b]}. \tag{A4}$$

Here V is the ENP volume and $\epsilon_b = 1$ is the background dielectric constant. In Eq. (A4), L_l is the static geometrical factor determined by the axis lengths of the ENP [50,51], with $L_a = 0.1736$ for the major axis and $L_{b(c)} = 0.4132$ for the minor axis in our case.

The optical response of the ENP can be characterized by the extinction cross section, as shown in Fig. 10. Red and black curves represent the extinction cross section of the ENP subjected to an external light field polarized parallel and vertical to the major axis, respectively. It is seen that the ENP shows obvious resonance near $f = 690$ THz and
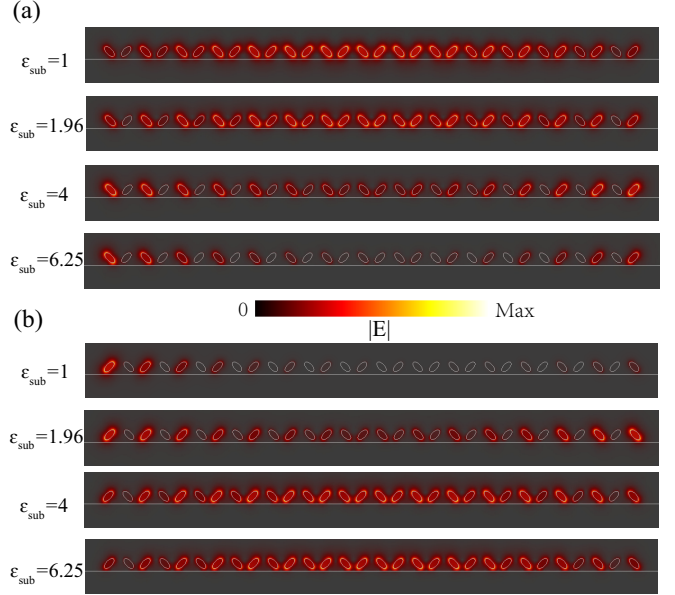

FIG. 11. (a), (b) The electric field intensity distribution of the edge (bulk) states represented by the red (blue) circles in Figs. 6(c) and 6(d), respectively.

$f = 850$ THz for the parallel and vertical polarized field, respectively. In particular, the resonance are separated far enough in the spectrum, which allows one to use α_a as the polarizability of the ENP when the operating frequency is near $f = 690$ THz. Therefore, the polarizability of the ENP is set to $\alpha = \alpha_a$ in the main text.

APPENDIX B: EXPRESSION FOR THE REFLECTING GREEN'S FUNCTION

The reflecting Green's function can be expressed as 1D integrations in k_ρ space as [40,52]

$$\overset{\leftrightarrow}{\mathbf{G}}_R(\mathbf{r}, \omega) = \int_0^\infty \frac{ik_\rho}{k_y}\left(\overset{\leftrightarrow S}{\mathbf{G}}_R - \frac{k_y^2}{k^2}\overset{\leftrightarrow P}{\mathbf{G}}_R\right) dk_\rho, \tag{B1}$$

where k_ρ is the component of the wave vector parallel to the substrate, $k_y = \sqrt{k^2 - k_\rho^2}$. Here $\mathbf{r} = (x, y, z)$ is the position vector between the dipole and observation point. In Eq. (B1), $\overset{\leftrightarrow S}{\mathbf{G}}_R$ and $\overset{\leftrightarrow P}{\mathbf{G}}_R$ are the terms involving the s and p waves, respectively. In Cartesian coordinates, the components of $\overset{\leftrightarrow S}{\mathbf{G}}_R$ and $\overset{\leftrightarrow P}{\mathbf{G}}_R$ are defined as

$$G_R^{S,xx} = \frac{R^S}{2}[J_0(k_\rho\rho) + J_2(k_\rho\rho)\cos(2\phi)],$$

$$G_R^{S,xz} = G_R^{S,zx} = -\frac{R^S}{2}J_2(k_\rho\rho)\sin(2\phi),$$

$$G_R^{S,zz} = \frac{R^S}{2}[J_0(k_\rho\rho) - J_2(k_\rho\rho)\cos(2\phi)],$$

$$G_R^{S,xy} = G_R^{S,yz} = G_R^{S,yx} = G_R^{S,zy} = G_R^{S,yy} = 0,$$

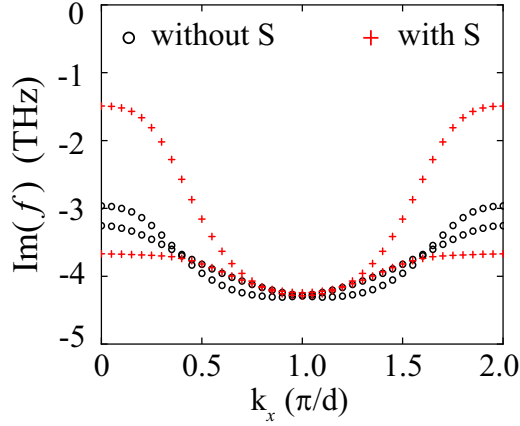$$G_R^{P,xx} = \frac{R^P}{2}[J_0(k_\rho\rho) - J_2(k_\rho\rho)\cos(2\phi)],$$

FIG. 12. Imaginary components of the band structures in Fig. 5(a).

$$G_R^{P,xz} = G_R^{P,zx} = \frac{R^P}{2}J_2(k_\rho\rho)\sin(2\phi),$$

$$G_R^{P,xy} = \frac{ik_\rho}{k_z}R^P J_1(k_\rho\rho)\cos(\phi),$$

$$G_R^{P,yx} = -\frac{ik_\rho}{k_z}R^P J_1(k_\rho\rho)\cos(\phi),$$

$$G_R^{P,yy} = -\frac{ik_\rho}{k_z}R^P J_1(k_\rho\rho),$$

$$G_R^{P,yz} = -\frac{ik_\rho}{k_z}R^P J_1(k_\rho\rho)\sin(\phi),$$

$$G_R^{P,zy} = \frac{ik_\rho}{k_z}R^P J_1(k_\rho\rho)\sin(\phi),$$

$$G_R^{P,zz} = \frac{R^P}{2}[J_0(k_\rho\rho) + J_2(k_\rho\rho)\cos(2\phi)], \quad (B2)$$
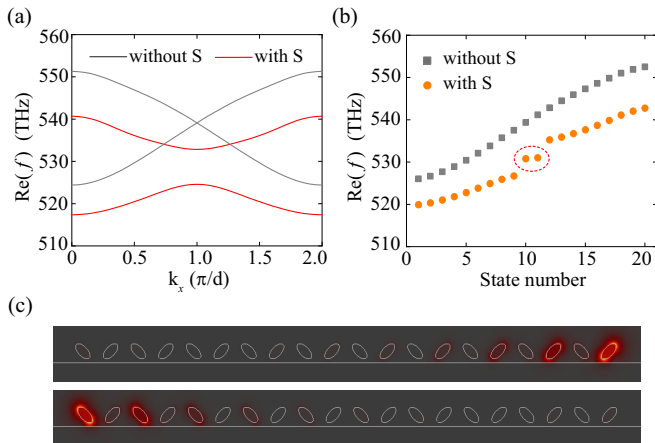

FIG. 13. FEM simulation results of the ENP chain embedded in a glass medium. (a) Band structures. (b) Eigenmodes of a finite-sized chain (ten unit cells) with and without the substrate, respectively. (c) The electric field intensity distribution of the two in-gap states encircled by the dashed oval in (b).

where

$$R^S = \frac{k_y - k_y^{sub}}{k_y + k_y^{sub}}e^{ik_y(2\Delta h + y)},$$

$$R^P = \frac{\epsilon_{sub}k_y - k_y^{sub}}{\epsilon_{sub}k_y + k_y^{sub}}e^{ik_y(2\Delta h + y)},$$

$$\rho = \sqrt{x^2 + z^2},$$

$$\phi = \arccos(x/\rho), \quad (B3)$$

with $k_y^{sub} = \sqrt{\epsilon_{sub}k^2 - k_\rho^2}$, Δh is the gap between the substrate and the ideal point dipole, and $J_n(K)$ is the Bessel function of order n. The integral method and computation of Eq. (B2) follows Ref. [45].

APPENDIX C: ELECTRIC FIELD DISTRIBUTION OF EDGE (BULK) STATES IN FIG. 6

Figures 11(a) and 11(b) show the electric field intensity distribution of the edge (bulk) states represented by the red (blue) circles in Figs. 6(c) and 6(d) in the main text, respectively. The bulk states in Fig. 11(a) transform into the edge states when the permittivity of the substrate increases from $\epsilon_{sub} = 1$ to $\epsilon_{sub} = 6.25$. On the contrary, the edge states in Fig. 11(b) transform into the bulk states. It is worth noting that the edge states tend to be degenerated and become increasingly asymmetric as ϵ_{sub} moves away from the phase transition point.

APPENDIX D: IMAGINARY COMPONENTS OF THE EIGENFREQUENCIES

Due to the retardation and radiative effects in the plasmonic system, all the eigenfrequencies presented in this paper have imaginary components. The imaginary parts are sufficiently small, and thus do not affect the emergence of topological states. As an example, Fig. 12 shows the imaginary parts of the eigenfrequencies, which correspond to the band structures shown in Fig. 5(a). These imaginary parts are less than 1% of the real parts of the eigenfrequencies. It is worth noting that the introduction of the substrate has led to a reduction of the imaginary components of the band structure.

APPENDIX E: THE INFLUENCE OF SURROUNDING MEDIUM

To experimentally realize the proposed system, one might consider using a surrounding medium other than air. The polarizability of the ENP is affected by the surrounding medium, as described by Eq. (A4). Consequently, the resonance frequency of the ENP varies depending on the surrounding medium. However, the coupling modulation effect among ENPs remains essentially the same whether in air or another isotropic surrounding medium. This is due to the asymmetric near-field profile of the ENPs, which is caused by their tilting towards the substrate and is unaffected by the surrounding medium. For instance, we consider embedding the ENP chain in a glass medium with the dielectric constant $\epsilon_b = 2.25$. The geometrical configurations of the chain and substrate are

consistent with those in Figs. 5(a)–5(c). Figure 13 shows the simulation results of the chain. The simulation clearly shows the band gap and in-gap edge states that appear in the presence of the substrate, similar to the results in air as shown in Fig. 5, except for a frequency shift from approximately 680 THz to 530 THz.

[1] F. D. M. Haldane and S. Raghu, Possible realization of directional optical waveguides in photonic crystals with broken time-reversal symmetry, Phys. Rev. Lett. **100**, 013904 (2008).

[2] Z. Wang, Y. Chong, J. D. Joannopoulos, and M. Soljacic, Observation of unidirectional backscattering-immune topological electromagnetic states, Nature (London) **461**, 772 (2009).

[3] L. Lu, J. D. Joannopoulos, and M. Soljacic, Topological photonics, Nat. Photon **8**, 821 (2014).

[4] T. Ozawa, H. M. Price, A. Amo, N. Goldman, M. Hafezi, L. Lu, M. C. Rechtsman, D. Schuster, J. Simon, O. Zilberberg, and I. Carusotto, Topological photonics, Rev. Mod. Phys. **91**, 015006 (2019).

[5] Z. Liu, G. Wei, and J.-J. Xiao, Geometric anisotropy induced higher-order topological insulators in nonsymmorphic photonic crystals, Phys. Rev. B **106**, 085415 (2022).

[6] G. Wei, Z. Liu, L. Wang, J. Song, and J.-J. Xiao, Coexisting valley and pseudo-spin topological edge states in photonic topological insulators made of distorted Kekule lattices, Photonics Res. **10**, 999 (2022).

[7] Z. Liu, G. Wei, H. Wu, and J.-J. Xiao, Mobius edge band and Weyl-like semimetal flat-band in topological photonic waveguide array by synthetic gauge flux, Nanophotonics **12**, 3481 (2023).

[8] C. W. Ling, M. Xiao, C. T. Chan, S. F. Yu, and K. H. Fung, Topological edge plasmon modes between diatomic chains of plasmonic nanoparticles, Opt. Express **23**, 2021 (2015).

[9] C. A. Downing and G. Weick, Topological collective plasmons in bipartite chains of metallic nanoparticles, Phys. Rev. B **95**, 125426 (2017).

[10] S. R. Pocock, X. Xiao, P. A. Huidobro, and V. Giannini, Topological plasmonic chain with retardation and radiative effects, ACS Photonics **5**, 2271 (2018).

[11] B. X. Wang and C. Y. Zhao, Topological phonon polaritons in one-dimensional non-Hermitian silicon carbide nanoparticle chains, Phys. Rev. B **98**, 165435 (2018).

[12] Q. Yan, E. Cao, Q. Sun, Y. Ao, X. Hu, X. Shi, Q. Gong, and H. Misawa, Near-field imaging and time-domain dynamics of photonic topological edge states in plasmonic nanochains, Nano Lett. **21**, 9270 (2021).

[13] Y. Zhang, R. P. H. Wu, L. Shi, and K. H. Fung, Second-order topological photonic modes in dipolar arrays, ACS Photonics **7**, 2002 (2020).

[14] M. Proctor, M. Blanco de Paz, D. Bercioux, A. Garcia-Etxarri, and P. A. Huidobro, Higher-order topology in plasmonic Kagome lattices, Appl. Phys. Lett. **118**, 091105 (2021).

[15] C.-R. Mann and E. Mariani, Topological transitions in arrays of dipoles coupled to a cavity waveguide, Phys. Rev. Res. **4**, 013078 (2022).

[16] L. Wang, R.-Y. Zhang, M. Xiao, D. Han, C. T. Chan, and W. Wen, The existence of topological edge states in honeycomb plasmonic lattices, New J. Phys. **18**, 103029 (2016).

[17] C.-R. Mann, T. J. Sturges, G. Weick, W. L. Barnes, and E. Mariani, Manipulating type-I and type-II dirac polaritons in cavity-embedded honeycomb metasurfaces, Nat. Commun. **9**, 2194 (2018).

[18] M. Honari-Latifpour and L. Yousefi, Topological plasmonic edge states in a planar array of metallic nanoparticles, Nanophotonics **8**, 799 (2019).

[19] M. Proctor, R. V. Craster, S. A. Maier, V. Giannini, and P. A. Huidobro, Exciting pseudospin-dependent edge states in plasmonic metasurfaces, ACS Photonics **6**, 2985 (2019).

[20] M. S. Rider, A. Buendia, D. R. Abujetas, P. A. Huidobro, J. A. Sanchez-Gil, and V. Giannini, Advances and prospects in topological nanoparticle photonics, ACS Photonics **9**, 1483 (2022).

[21] Á. Buendía, J. A. Sanchez-Gil, and V. Giannini, Exploiting oriented field projectors to open topological gaps in plasmonic nanoparticle arrays, ACS Photonics **10**, 464 (2023).

[22] A. Poddubny, A. Miroshnichenko, A. Slobozhanyuk, and Y. Kivshar, Topological Majorana states in zigzag chains of plasmonic nanoparticles, ACS Photonics **1**, 101 (2014).

[23] A. P. Slobozhanyuk, A. N. Poddubny, A. E. Miroshnichenko, P. A. Belov, and Y. S. Kivshar, Subwavelength topological edge states in optically resonant dielectric structures, Phys. Rev. Lett. **114**, 123901 (2015).

[24] L. Lin, S. Kruk, Y. Ke, C. Lee, and Y. Kivshar, Topological states in disordered arrays of dielectric nanoparticles, Phys. Rev. Res. **2**, 043233 (2020).

[25] L. Zhang, X.-M. Wang, X.-M. Qiu, Z. Wang, and J.-Y. Yan, Light controlled topological plasmonics in a graphene lattice arrayed by metal nanoparticles, Phys. Rev. B **108**, 085402 (2023).

[26] C. A. Downing, T. J. Sturges, G. Weick, M. Stobińska, and L. Martín-Moreno, Topological phases of polaritons in a cavity waveguide, Phys. Rev. Lett. **123**, 217401 (2019).

[27] C.-R. Mann, S. A. R. Horsley, and E. Mariani, Tunable pseudo-magnetic fields for polaritons in strained metasurfaces, Nat. Photon. **14**, 669 (2020).

[28] D. Zhao, Z. Wang, L. Yang, Y. Zhong, X. Xi, Z. Zhu, M. Gong, Q. Tu, Y. Meng, B. Yan, C. Shang, and Z. Gao, Observation of tunable topological polaritons in a cavity waveguide, arXiv:2401.10450.

[29] R. S. Savelev and M. A. Gorlach, Topological states in arrays of optical waveguides engineered via mode interference, Phys. Rev. B **102**, 161112(R) (2020).

[30] A. V. Gorbach, J. Beer, and A. Souslov, Topological edge states in equidistant arrays of lithium niobate nano-waveguides, Opt. Lett. **48**, 1982 (2023).

[31] G. Kurganov, D. Dobrykh, E. Puhtina, I. Yusupov, A. Slobozhanyuk, Y. S. Kivshar, and D. Zhirihin, Temperature control of electromagnetic topological edge states, Appl. Phys. Lett. **120**, 233105 (2022).

[32] S.-X. Xia, D. Zhang, X. Zhai, L.-L. Wang, and S.-C. Wen, Phase-controlled topological plasmons in 1D graphene nanoribbon array, Appl. Phys. Lett. **123**, 101102 (2023).

[33] J. van de Groep and A. Polman, Designing dielectric resonators on substrates: Combining magnetic and electric resonances, Opt. Express **21**, 26285 (2013).

[34] J.-W. Dong and Z.-L. Deng, Direct eigenmode analysis of plasmonic modes in metal nanoparticle chain with layered medium, Opt. Lett. **38**, 2244 (2013).

[35] P. J. Compaijen, V. A. Malyshev, and J. Knoester, Surface-mediated light transmission in metal nanoparticle chains, Phys. Rev. B **87**, 205437 (2013).

[36] W. Liu and E. Mcleod, Fast and accurate electromagnetic field calculation for substrate-supported metasurfaces using the discrete dipole approximation, Nanophotonics **12**, 4157 (2023).

[37] J. Xiang, Y. Xu, J. Chen, and S. Lan, Tailoring the spatial localization of bound state in the continuum in plasmonic-dielectric hybrid system, Nanophotonics **9**, 133 (2020).

[38] R. Kolkowski and A. Shevchenko, Enabling infinite Q factors in absorbing optical systems, Nanophotonics **12**, 3443 (2023).

[39] Y. Han, L. Xiong, J. Shi, and G. Li, Observation of tunable accidental bound state in the continuum in silicon nanodisk array, Nanophotonics **13**, 1603 (2024).

[40] R. Jones, J. A. Needham, I. Lesanovsky, F. Intravaia, and B. Olmos, Modified dipole-dipole interaction and dissipation in an atomic ensemble near surfaces, Phys. Rev. A **97**, 053841 (2018).

[41] D. Fernández-Fernández and A. González-Tudela, Tunable directional emission and collective dissipation with quantum metasurfaces, Phys. Rev. Lett. **128**, 113601 (2022).

[42] A. Noual, R. Akiki, Y. Pennec, E. H. El Boudouti, and B. Djafari-Rouhani, Surface acoustic waves-localized plasmon interaction in pillared phononic crystals, Phys. Rev. Appl. **13**, 024077 (2020).

[43] M. Quinten, A. Leitner, J. Krenn, and F. Aussenegg, Electromagnetic energy transport via linear chains of silver nanoparticles, Opt. Lett. **23**, 1331 (1998).

[44] A. Ghatak and T. Das, New topological invariants in non-Hermitian systems, J. Phys.: Condens. Matter **31**, 263001 (2019).

[45] M. Paulus, P. Gay-Balmaz, and O. J. F. Martin, Accurate and efficient computation of the Green's tensor for stratified media, Phys. Rev. E **62**, 5797 (2000).

[46] K. H. Fung and C. T. Chan, Plasmonic modes in periodic metal nanoparticle chains: A direct dynamic eigenmode analysis, Opt. Lett. **32**, 973 (2007).

[47] L. Chu, Z. Li, H. Zhu, F. Ren, and F. Chen, Second-harmonic generation of embedded plasmonic nanoparticle arrays via interparticle coupling, Appl. Phys. Lett. **120**, 073104 (2022).

[48] N. Wang, R.-Y. Zhang, Q. Guo, S. Wang, G. P. Wang, and C. T. Chan, Optical pulling using topologically protected one way transport surface-arc waves, Phys. Rev. B **105**, 014104 (2022).

[49] H. U. Yang, J. D'Archangel, M. L. Sundheimer, E. Tucker, G. D. Boreman, and M. B. Raschke, Optical dielectric function of silver, Phys. Rev. B **91**, 235137 (2015).

[50] A. Moroz, Depolarization field of spheroidal particles, J. Opt. Soc. Am. B **26**, 517 (2009).

[51] Y. Hadad and B. Z. Steinberg, Magnetized spiral chains of plasmonic ellipsoids for one-way optical waveguides, Phys. Rev. Lett. **105**, 233904 (2010).

[52] L. Novotny and B. Hecht, *Principles of Nano-Optics*, 2nd ed. (Cambridge University Press, Cambridge, UK, 2012).